

Geometry-Based Modeling of Wideband Industrial Indoor Radio Propagation Channels

Yun Ai^{1,2}, Bjørn Olav Hogstad¹, Michael Cheffena¹, Matthias Pätzold³

¹Norwegian University of Science and Technology, N-2815 Gjøvik, Norway, ²University of Oslo, N-0373 Oslo, Norway,

³University of Agder, N-4898 Grimstad, Norway

Email: {yun.ai, bjorn.hogstad, michael.cheffena}@ntnu.no, matthias.patzold@uia.no

Abstract—In this paper, we present a geometrical scattering model for a typical class of industrial indoor environments. The proposed industrial reference model takes into account scattering components arising from metallic structures and the surrounding walls of the investigated environment. Starting from the geometrical scattering model, we derive the analytical expressions of the probability density function (PDF) of the angle of arrival (AoA), PDF of the time of arrival (ToA), and the autocorrelation function (ACF) in the frequency domain. The obtained results reveal a large difference between industrial channels and other home and office environments. The theoretical results of the reference model are validated by simulation results of a channel simulator designed by employing the sum-of-cisoids (SOC) principle. The proposed channel model is useful for the design and performance evaluation of wireless communication systems operating in industrial environments.

Index Terms—Industrial indoor channels, wideband channel model, multipath propagation, geometry-based channel model.

I. INTRODUCTION

In recent years, there has been a growing interest from industrial manufacturing companies to incorporate wireless communications in their production process. Compared to traditional wired communication systems, the wireless solution has the advantage in terms of deployment flexibility, potential in data collection, enabling remote control, etc. [1].

It is known that the wave propagation characteristics in industrial environments are different from those in offices and residential indoor environments due to a number of factors including the presence of highly reflective metallic structures (machinery) [2]. The successful design and deployment of wireless communication systems in industrial settings necessitates a good knowledge of the propagation characteristics of industrial channels. To this end, a number of measurement campaigns have been conducted in various industrial environments over the past few years and empirical channel models have been developed based on field measurements [1]–[3]. However, the nature of empirical models implies that they are only applicable and accurate for environments sharing the same channel characteristics with those where the measurements were performed. This limits the usage of empirical channel models. Ray tracing (RT) is an alternative channel modeling technique, which evaluates all propagation paths as they interact with the surrounding environment based on the geometrical theory of diffraction [4]. Nevertheless, the accuracy of RT models largely depends on the detailed

knowledge of the geometrical and dielectric properties of the site, which often results in large, sometimes prohibitive, computational cost and simulation time.

To cope with the drawbacks of the aforementioned models and to provide sufficiently accurate channel characterization of a wide range of scenarios at reasonable computational cost, a geometry-based approach utilizing the statistical distribution of the scatterers from the scenario of interest has been proposed to model various propagation channels. In [5], a vehicle-to-vehicle channel was analyzed by placing an ensemble of point scatterers according to a site-specific statistical distribution. In [6], the approach was used to model shallow underwater acoustic channels under the condition of rough surface and bottom scattering. A multiple-input multiple-output (MIMO) mobile-to-mobile fading channel model was derived under the geometrical two-ring scattering assumption in [7].

In this paper, we apply the geometry-based modeling approach to model the wideband channel in typical industrial indoor environments. The remainder of this paper is organized as follows: Section II describes the industrial geometrical scattering model and the underlying industrial setting. In Section III, some of the characteristic quantities describing the wideband channel are derived, such as the PDF of the AoA, PDF of the ToA, and the frequency correlation function (FCF). The numerical results are presented and discussed in Section IV. Section V concludes the paper.

II. GEOMETRICAL SCATTERING ASSUMPTION FOR INDUSTRIAL INDOOR CHANNELS

Observations in a large number of factories revealed that there are some common characteristics in the layout of many manufacturing sites (especially in modern plants with automated production or processing lines): the equipments are often installed along multiple parallel production lines with straight aisles in between them for passing workers or materials. In this case, most of the multipath components might be due to reflections from the building walls as well as reflections from the production lines. The scatterer density along each production column is usually high and decays exponentially with distance to the neighboring production line. This may suggest that the scatterer density in the industrial environment might be described using multiple exponential decay functions. In addition, the equipment is in most cases metallic, producing a higher degree of scattering than concrete



Fig. 1: A typical industrial workshop with parallel automated production lines.

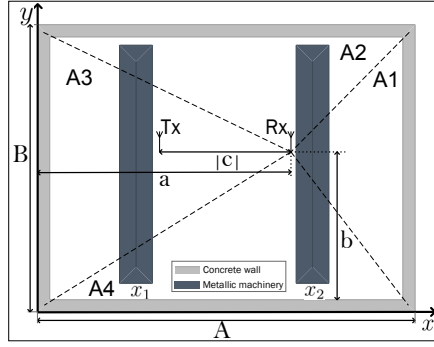


Fig. 2: The geometrical abstraction of the industrial environment as shown in Fig. 1.

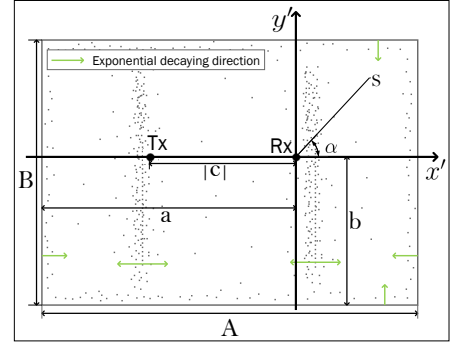


Fig. 3: The industrial geometry-based model in the Cartesian coordinate system.

walls (see Figs. 1 and 2). From the above statements, we make the following assumptions on our industrial channel model. Firstly, we assume that an infinite number of randomly distributed scatterers in the three dimensional (3D) environment are projected onto a 2D horizontal plane. It should be noted that while the real environment is intrinsically 3D, the 2D model can provide meaningful results with orders of magnitude less complexity. Secondly, the density of the scatterers stemming from each production line decays exponentially with the distance from the production line in the two directions perpendicular to it. The density of the scatterers stemming from the surrounding walls also decays exponentially with the distance from the walls (see Fig. 3). The overall density is the superposition of the scatterer densities resulting from all production lines and the surrounding walls. The exponential distribution has also been used to model the scatterers around the base station in outdoor cellular scenarios, where the results were in good agreement with the measurement data [8].

The geometrical abstraction of the modelled industrial scenario is illustrated in Fig. 2. The rectangle represents an industrial room of length A and width B . The receiver (Rx) is located at position (a, b) and the transmitter (Tx) is

located at position $(a + c, b)$. For simplicity, we assume single-bounce scattering, i.e., the emitted waves are only bounced once by scatterers before being received by the Rx. Inside the room, N parallel production lines are placed at positions x_1, x_2, \dots, x_N . The parameters $x_0 = 0$ and $x_{N+1} = A$ represent the positions of the two walls perpendicular to the x -axis (see Fig. 2). The position of a scatterer S is given by a pair of random variables (\mathbf{x}, \mathbf{y}) . Under these assumptions on the distribution of scatterers, the PDFs of the random variables \mathbf{x} and \mathbf{y} , denoted by $f_{\mathbf{x}}(x)$ and $f_{\mathbf{y}}(y)$, are given in (1) and (2), respectively, at the bottom of this page. Assuming independence between \mathbf{x} and \mathbf{y} , the joint PDF of the scatterer density taking account of the effects from the machines and surrounding walls can be expressed as

$$f_{\mathbf{x},\mathbf{y}}(x, y) = f_{\mathbf{x}}(x) \cdot f_{\mathbf{y}}(y). \quad (5)$$

III. STATISTICAL CHARACTERIZATION OF THE INDUSTRIAL CHANNEL MODEL

In this section, we derive the PDF of the AoA, PDF of the ToA, power delay profile (PDP), and the FCF of the industrial channel model based on the geometrical assumptions described in Section II.

$$f_{\mathbf{x}}(x) = \begin{cases} P_1 \cdot \left[\sum_{n=0}^N e^{-w_n^+(x-x_n)} \mathbf{1}(x_n, x_{n+1}) + \sum_{n=1}^N e^{w_n^-(x-x_n)} \mathbf{1}(x_{n-1}, x_n) + e^{w_0^-(x-A)} \mathbf{1}(x_N, A) + C_1 \right] & \text{if } x \in (0, A) \\ 0 & \text{otherwise} \end{cases} \quad (1)$$

$$f_{\mathbf{y}}(y) = \begin{cases} P_2 \cdot \left[e^{-k_0^+ y} + e^{k_0^-(y-B)} + C_2 \right] & \text{if } y \in (0, B) \\ 0 & \text{otherwise} \end{cases} \quad (2)$$

where $w_n \geq 0$ ($n = 0, 1, \dots, N$) and $k_0 \geq 0$ are the decaying factors of the exponential distributions and a larger number indicates faster decay (e.g., objects of different materials or densities might be given different values of decaying factor). The superscripts of w_n and k_0 ('+' or '-') indicate the decaying direction. The symbol $\mathbf{1}(v_1, v_2)$ represents the indicator function, which equals to 1 within the range (v_1, v_2) and 0 elsewhere. The parameters C_n and P_n ($n = 1, 2$) are ratios with P_1 and P_2 enforcing the following equalities: $\int_0^A f_{\mathbf{x}}(x) dx = 1$ and $\int_0^B f_{\mathbf{y}}(y) dy = 1$. They are computed as follows

$$P_1 = \left[\sum_{n=0}^N \frac{1 - e^{-w_n^+(x_n - x_{n+1})}}{w_n^+} + \sum_{n=1}^N \frac{1 - e^{-w_n^-(x_{n-1} - x_n)}}{w_n^-} + \frac{1 - e^{-w_0^-(x_N - A)}}{w_0^-} + C_1 A \right]^{-1} \quad (3)$$

$$P_2 = \left[\frac{1 - e^{-k_0^+ B}}{k_0^+} + \frac{1 - e^{-k_0^- B}}{k_0^-} + C_2 B \right]^{-1}. \quad (4)$$

A. Derivation of the PDF of the AoA

To simplify the derivation of the AoA and ToA, we shift the origin of the Cartesian coordinate system in Fig. 2 to the position of the Rx (see Fig. 3). Within the shifted coordinate system, the PDF of the scatterer density, denoted by $f_{\mathbf{x}',\mathbf{y}'}(x', y')$, is given as

$$\begin{aligned} f_{\mathbf{x}',\mathbf{y}'}(x', y') &= f_{\mathbf{x}'}(x') \cdot f_{\mathbf{y}'}(y') = f_{\mathbf{x},\mathbf{y}}(x' + a, y' + b) \\ &= f_{\mathbf{x}}(x' + a) \cdot f_{\mathbf{y}}(y' + b) \end{aligned} \quad (6)$$

where $f_{\mathbf{x}}(\cdot)$ and $f_{\mathbf{y}}(\cdot)$ are given in (1) and (2), respectively.

Next, we derive the joint PDF of the propagation path length D and the AoA α from the distribution of the scatterers. The propagation path length D is the overall propagation length from the Tx to the Rx under the single-bounce scattering assumption. The AoA α and propagation path length D are given by

$$\alpha = \arctan\left(\frac{y'}{x'}\right) \quad (7)$$

$$D = \sqrt{(x'^2 + y'^2) - 2c \cdot \cos(\alpha) \cdot \sqrt{x'^2 + y'^2} + c^2} + \sqrt{x'^2 + y'^2}. \quad (8)$$

The joint PDF $f_{D,\alpha}(D, \alpha)$ of the propagation path length D and the AoA α can be obtained by applying the concept of transformation of random variables to the relationship between (x', y') and (D, α) [9, pp. 182–193], which results in

$$\begin{aligned} f_{D,\alpha}(D, \alpha) &= |J(D, \alpha)| \cdot f_{\mathbf{x}',\mathbf{y}'}(D, \alpha) \\ &= \left| \begin{array}{cc} \frac{\partial y'}{\partial D} & \frac{\partial y'}{\partial \alpha} \\ \frac{\partial x'}{\partial D} & \frac{\partial x'}{\partial \alpha} \end{array} \right| \cdot f_{\mathbf{x}'}(D, \alpha) \cdot f_{\mathbf{y}'}(D, \alpha) \end{aligned} \quad (9)$$

where

$$|J(D, \alpha)| = \frac{[D^2 - 2Dc \cdot \cos(\alpha) + c^2] (D^2 - c^2)}{4 [D - c \cdot \cos(\alpha)]^3} \quad (10)$$

$$f_{\mathbf{x}'}(D, \alpha) = f_{\mathbf{x}'}\left(\frac{(D^2 - c^2) \cdot \cos(\alpha)}{2 [D - c \cdot \cos(\alpha)]}\right) \quad (11)$$

$$f_{\mathbf{y}'}(D, \alpha) = f_{\mathbf{y}'}\left(\frac{(D^2 - c^2) \cdot \sin(\alpha)}{2 [D - c \cdot \cos(\alpha)]}\right). \quad (12)$$

Then, the PDF $f_{\alpha}(\alpha)$ of the AoA α can be obtained by integrating the joint PDF $f_{D,\alpha}(D, \alpha)$ over the range of D , i.e.,

$$f_{\alpha|I_D}(\alpha) = \int_{D \in I_D} f_{D,\alpha}(D, \alpha) dD \quad (13)$$

where $I_D = (D_1^*, D_2^*]$. The parameters D_1^* and D_2^* represent the minimum and maximum propagation path length, respectively. With some straightforward geometrical derivations, it can be shown that $D_1^* = |c|$ and the value of $D_2^* = D_2^*(\alpha)$ is given by (14) and (15).

Note that the four angles α_1^* , α_2^* , α_3^* , and α_4^* in (15) partition the scattering region of the industrial room into four areas, as illustrated in Fig. 2.

$$D_2^*(\alpha) = \begin{cases} \frac{A-a}{\cos(\alpha)} + \sqrt{\left[\frac{A-a}{\cos(\alpha)}\right]^2 - 2c(A-a) + c^2} & \text{if } \alpha \in (\alpha_1^*, \alpha_2^*] \\ \frac{B-b}{\sin(\alpha)} + \sqrt{\left[\frac{B-b}{\sin(\alpha)}\right]^2 - 2c(B-b) \cdot \cot(\alpha) + c^2} & \text{if } \alpha \in (\alpha_2^*, \alpha_3^*] \\ \frac{-a}{\cos(\alpha)} + \sqrt{\left[\frac{a}{\cos(\alpha)}\right]^2 + 2ca + c^2} & \text{if } \alpha \in (\alpha_3^*, \alpha_4^*] \\ \frac{-b}{\sin(\alpha)} + \sqrt{\left[\frac{b}{\sin(\alpha)}\right]^2 + 2cb \cdot \cot(\alpha) + c^2} & \text{if } \alpha \in (\alpha_4^*, 2\pi + \alpha_1^*] \end{cases} \quad (14)$$

where

$$\begin{aligned} \alpha_1^* &= -\arctan\left(\frac{b}{A-a}\right), & \alpha_2^* &= \arctan\left(\frac{B-b}{A-a}\right) \\ \alpha_3^* &= \pi - \arctan\left(\frac{B-b}{a}\right), & \alpha_4^* &= \pi + \arctan\left(\frac{b}{a}\right). \end{aligned} \quad (15)$$

B. Derivation of the PDF of the ToA

The ToA τ and the propagation path length D are related by

$$\tau = \frac{D - |c|}{v_0} \quad (16)$$

where v_0 is the speed of light.

By applying the concept of transformation of random variables again [9, pp. 182–193], we obtain the PDF $f_{\tau}(\tau)$ of the ToA τ from the PDF $f_D(D)$ of the propagation length D as

$$f_{\tau}(\tau) = v_0 \cdot f_D(v_0\tau + |c|). \quad (17)$$

The PDF $f_D(D)$ of the propagation path length D can be derived from the joint PDF $f_{D,\alpha}(D, \alpha)$ in (9)–(12) as follows

$$f_D|_{I_{\alpha}}(D) = \int_{\alpha \in I_{\alpha}} f_{D,\alpha}(D, \alpha) d\alpha. \quad (18)$$

The integral in (18) can be solved by reusing the relation between D_2^* and α in (14) (see Appendix A). The analytical expressions for $f_D(D)$ and the integral interval I_{α} are given in (19)–(21) on the next page.

C. Derivation of the FCF

Let the total power of the received multipath components be P_0 . Then, the following equation holds: $\int_0^{+\infty} A_c(\tau) d\tau = P_0$, where $A_c(\tau)$ is the PDP. By using the property $\int_0^{+\infty} f_{\tau}(\tau) d\tau = 1$ and $A_c(\tau) \propto f_{\tau}(\tau)$, we can obtain the following relation:

$$A_c(\tau) = P_0 \cdot f_{\tau}(\tau). \quad (22)$$

Then, utilizing the relationship between the PDP and the ACF, i.e., $\mathcal{F}[A_c(\tau)] \stackrel{\tau \leftrightarrow \Delta f}{=} A_c(\Delta f, \Delta t = 0)$, where $A_c(\Delta f, \Delta t)$ is the ACF in the frequency and time domain [10, p. 117] and $\mathcal{F}(\cdot)$ denotes the Fourier transform, we can obtain the FCF $A_c(\Delta f)$:

$$A_c(\Delta f) = P_0 \cdot \int_0^{+\infty} f_{\tau}(\tau) e^{-j2\pi\Delta f\tau} d\tau. \quad (23)$$

$$f_{\mathbf{D}}(D) = \begin{cases} f_{\mathbf{D}|I_{\alpha}=(-\pi,\pi)}(D) & \text{if } D \in (|c|, D_6] \\ f_{\mathbf{D}|I_{\alpha}=(-\pi,\alpha_1)}(D) + f_{\mathbf{D}|I_{\alpha}=(\alpha_2,\pi)}(D) & \text{if } D \in (D_6, D_8] \\ f_{\mathbf{D}|I_{\alpha}=(-\pi,\alpha_3)}(D) + f_{\mathbf{D}|I_{\alpha}=(\alpha_4,\alpha_1)}(D) + f_{\mathbf{D}|I_{\alpha}=(\alpha_2,\pi)}(D) & \text{if } D \in (D_8, D_5] \\ f_{\mathbf{D}|I_{\alpha}=(-\pi,\alpha_3)}(D) + f_{\mathbf{D}|I_{\alpha}=(\alpha_4,\alpha_5)}(D) + f_{\mathbf{D}|I_{\alpha}=(\alpha_6,\alpha_1)}(D) + f_{\mathbf{D}|I_{\alpha}=(\alpha_2,\pi)}(D) & \text{if } D \in (D_5, D_1] \\ f_{\mathbf{D}|I_{\alpha}=(-\pi,\alpha_3)}(D) + f_{\mathbf{D}|I_{\alpha}=(\alpha_4,\alpha_5)}(D) + f_{\mathbf{D}|I_{\alpha}=(\alpha_2,\pi)}(D) & \text{if } D \in (D_1, D_2] \\ f_{\mathbf{D}|I_{\alpha}=(-\pi,\alpha_3)}(D) + f_{\mathbf{D}|I_{\alpha}=(\alpha_2,\pi)}(D) & \text{if } D \in (D_2, D_7] \\ f_{\mathbf{D}|I_{\alpha}=(\alpha_8,\alpha_3)}(D) + f_{\mathbf{D}|I_{\alpha}=(\alpha_2,\alpha_7)}(D) & \text{if } D \in (D_7, D_3] \\ f_{\mathbf{D}|I_{\alpha}=(\alpha_8,\alpha_3)}(D) & \text{if } D \in (D_3, D_4] \end{cases} \quad (19)$$

where

$$\begin{aligned} \alpha_1 &= 2 \arctan\left(\frac{D-c}{2(B-b)} - \sqrt{\frac{(D-c)^2}{4(B-b)^2} - \frac{D-c}{D+c}}\right), & \alpha_2 &= 2 \arctan\left(\frac{D-c}{2(B-b)} + \sqrt{\frac{(D-c)^2}{4(B-b)^2} - \frac{D-c}{D+c}}\right) \\ \alpha_3 &= -2 \arctan\left(\frac{D-c}{2b} + \sqrt{\frac{(D-c)^2}{4b^2} - \frac{D-c}{D+c}}\right), & \alpha_4 &= -2 \arctan\left(\frac{D-c}{2b} - \sqrt{\frac{(D-c)^2}{4b^2} - \frac{D-c}{D+c}}\right) \\ \alpha_5 &= -\arccos \frac{2D(A-a)}{D^2-c^2+2c(A-a)}, & \alpha_6 &= \arccos \frac{2D(A-a)}{D^2-c^2+2c(A-a)}, & \alpha_7 &= \arccos \frac{-2Da}{D^2-c^2+2ca}, & \alpha_8 &= -\arccos \frac{-2Da}{D^2-c^2+2ca} \end{aligned} \quad (20)$$

and

$$\begin{aligned} D_1 &= \sqrt{(A-a)^2 + (B-b)^2} + \sqrt{(A-a-c)^2 + (B-b)^2}, & D_2 &= \sqrt{(A-a)^2 + b^2} + \sqrt{(A-a-c)^2 + b^2} \\ D_3 &= \sqrt{a^2 + (B-b)^2} + \sqrt{(a+c)^2 + (B-b)^2}, & D_4 &= \sqrt{a^2 + b^2} + \sqrt{(a+c)^2 + b^2} \\ D_5 &= 2(A-a) - c, & D_6 &= \sqrt{4(B-b)^2 + c^2}, & D_7 &= 2a + c, & D_8 &= \sqrt{4b^2 + c^2}. \end{aligned} \quad (21)$$

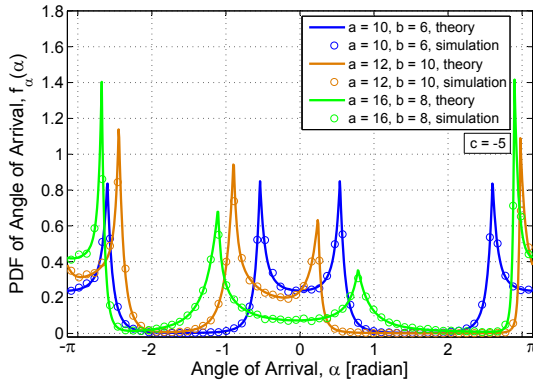


Fig. 4: PDF $f_{\alpha}(\alpha)$ of AoA α for different Tx and Rx positions.

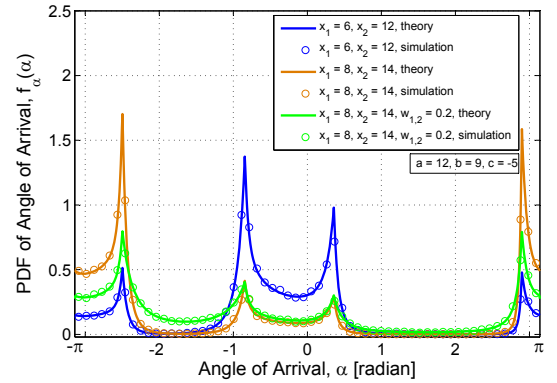


Fig. 5: PDF $f_{\alpha}(\alpha)$ of AoA α for different machine positions.

It should be noted that there exists no closed-form solution for the integral (23). Thus, it needs to be computed numerically.

IV. NUMERICAL AND SIMULATION RESULTS

This section provides the numerical and simulation results for the statistical characteristics of the industrial channel model analyzed in Section III. The corresponding simulation model is designed by applying the SOC method [11, pp. 126–134]. The parameters of the SOC channel simulator are computed using the Modified Method of Equal Areas [12]. Unless specified, the simulation results in this section are based on the following geometry: an industrial indoor room with length $A = 20$ m and width $B = 12$ m. Two lines of machines are placed in the room at positions $x_1 = 6$ m and $x_2 = 14$ m (see Fig. 2). The weighting factors of the exponential decaying distribution functions in (1)–(4) are set as $w_n^{\pm} = 0.6$ ($n = 1, 2$) for the metallic machineries, $w_0^{\pm} = k_0^{\pm} = 1.2$ for the surrounding walls and the ratios C_n ($n = 1, 2$) being 0.122 and 0.3286,

respectively, with this setting. Typical values of the decaying factors in real industrial environments can be obtained by fitting the theoretical statistics of the proposed channel model to the statistics of measured industrial channels by optimizing the key parameters of the channel model, similar to what was done in [13]. This work will not be included in this paper due to the page limit and will thus be left for future work.

The theoretical results of the PDF $f_{\alpha}(\alpha)$ of the AoA α are compared with Monte Carlo simulations in Figs. 4 and 5 for different positions of the Tx, Rx, and machinery. As expected, a symmetrical shape of the PDF $f_{\alpha}(\alpha)$ is observed if the Rx is located at the center of the industrial room (i.e., $a = 10, b = 6$). It can also be observed that the incoming waves are highly non-uniformly distributed in an industrial environment. This is in contrast to the AoA distribution of indoor office environments, where the waves arrive mainly in the direction connecting the Tx and Rx [14]. The distribution

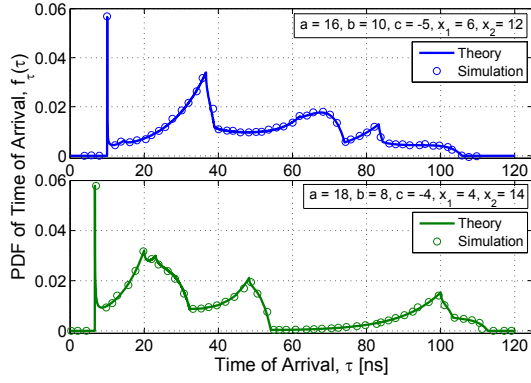


Fig. 6: PDF $f_\tau(\tau)$ of ToA τ for different geometries.

$f_\alpha(\alpha)$ of the AoA α is quite variable and highly depends on the geometry, link configuration, and distribution of the scatterers inside the investigated environment.

The PDF $f_\tau(\tau)$ of the ToA τ under two different geometries is shown in Fig. 6. The results show that the incoming waves arrive in several clearly identifiable clusters, which is in accordance with field measurements in industrial environments [3] and the assumptions of the well-known Saleh-Valenzuela (S-V) model [15]. The arrival time and shape of each cluster depend highly on the corresponding link configuration and site geometry. The simulated shapes of the ToA PDF $f_\tau(\tau)$ are also significantly different from those obtained with the elliptical or circular scattering models proposed for the simulation of outdoor cellular channels, where the PDF of the ToA has roughly the shape of a negative exponential function [8].

Figure 7 shows the absolute value of the FCF $A_c(\Delta f)$ for different Tx positions with fixed Rx position. A good match can be observed between the FCF of the reference model and the simulation model. From Fig. 7, we can see that the channel coherence bandwidth increases as the Tx moves towards the Rx. This is in concert with industrial measurements, where the delay spread was observed to increase with increasing Tx-Rx distance [3].

V. CONCLUSION

In this paper, we proposed a wideband channel model for a typical indoor industrial environment. The reference channel model is derived under the assumption that an infinite number of scatterers are exponentially distributed due to metallic machineries and walls within the horizontal plane of a rectangular industrial room. The statistical properties of the proposed channel model have been investigated. Analytical expressions have been derived for the PDF of the AoA and ToA, and the FCF. It has been shown that the waves arrive in clusters, where the link configuration and the geometry of the industrial room have significant influence on the channel characteristics. The reference model can be efficiently simulated by utilizing the SOC approach, which has the advantage of reduced realization expenditure. The proposed model is helpful for the design and evaluation of robust wireless systems for industrial applications. Future work includes verifying the developed model using measurements and extracting typical values of the model parameters.

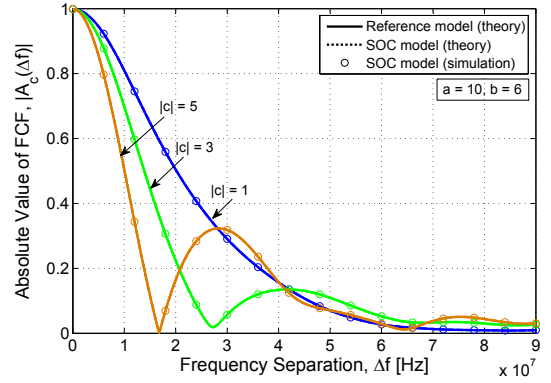


Fig. 7: Absolute value of FCF $|A_c(\Delta f)|$ for different Tx-Rx distances.

APPENDIX A

DERIVATION OF D_i AND α_i ($i = 1, 2, \dots, 8$) IN (19) - (21)

In this section, we determine the range of the maximum propagation distance of the plane wave for the four scattering areas illustrated in Fig. 2, i.e., the values of D_i ($i = 1, 2, \dots, 8$) in (21) and the corresponding integral limits α_i ($i = 1, 2, \dots, 8$) in (20). The rectangular industrial room is partitioned into four areas by the four angles α_i^* ($i = 1, 2, 3, 4$) given in (15).

Area A1: $\alpha_1^* < \alpha \leq \alpha_2^*$

It can be observed from (14) that $D_2^*(\alpha)$ is a monotonic increasing function if $\alpha \in (0, \alpha_2^*]$. The maximum value is taken at $\alpha = \alpha_2^*$ and the minimum value at $\alpha = 0$, i.e.,

$$D_1 = \max(D_2^*(\alpha)) = D_2^*(\alpha)|_{\alpha=\alpha_2^*} = \sqrt{(A-a)^2 + (B-b)^2} + \sqrt{(A-a-c)^2 + (B-b)^2} \quad (\text{A.1})$$

$$D_5 = \min(D_2^*(\alpha)) = D_2^*(\alpha)|_{\alpha=0} = 2(A-a) - c. \quad (\text{A.2})$$

It can also be seen that $D_2^*(\alpha)$ is a monotonic decreasing function within $(\alpha_1^*, 0]$. Thus, the maximum D_2^* within this range is given by

$$D_2 = \max(D_2^*(\alpha)) = D_2^*(\alpha)|_{\alpha=\alpha_1^*} = \sqrt{(A-a)^2 + b^2} + \sqrt{(A-a-c)^2 + b^2}. \quad (\text{A.3})$$

Area A2: $\alpha_2^* < \alpha \leq \alpha_3^*$

If the AoA α is within the range $(\alpha_2^*, \alpha_3^*]$, we obtain the fixed angle $\alpha = \pi + \arctan \frac{2(B-b)}{c}$ by setting the first derivative of the function $D_2^*(\alpha)$, $\alpha \in (\alpha_2^*, \alpha_3^*]$, to zero. The second derivative of $D_2^*(\alpha)$ being positive indicates that $D_2^*(\alpha)$ has a minimum value at $\alpha = \pi + \arctan \frac{2(B-b)}{c}$, i.e.,

$$D_6 = \min(D_2^*(\alpha)) = D_2^*(\alpha)|_{\alpha=\pi+\arctan \frac{2(B-b)}{c}} = \sqrt{4(B-b)^2 + c^2}. \quad (\text{A.4})$$

If $\alpha \in (\pi + \arctan \frac{2(B-b)}{c}, \alpha_3^*]$, the function $D_2^*(\alpha)$ turns out to be a monotonic increasing function. Thus, $D_2^*(\alpha)$ has

a maximum value at $\alpha = \alpha_3^*$, i.e.,

$$D_3 = \max(D_2^*(\alpha)) = D_2^*(\alpha)|_{\alpha=\alpha_3^*} = \sqrt{a^2 + (B-b)^2} + \sqrt{(a+c)^2 + (B-b)^2}. \quad (\text{A.5})$$

The function $D_2^*(\alpha)$ is a monotonic decreasing function with respect to α in the range $(\alpha_2^*, \pi + \arctan \frac{2(B-b)}{c})$, which means that $D_2^*(\alpha) < D_1$ within this range.

Area A3: $\alpha_3^* < \alpha \leq \pi$ and $-\pi < \alpha \leq \alpha_4^* - 2\pi$

It is found that $D_2^*(\alpha)$ is a monotonic decreasing function within the range $(\alpha_3^*, \pi]$ by studying its first and second derivatives. Thus, we have $D_7 \leq D_2^*(\alpha) < D_3$, where

$$D_7 = \min(D_2^*(\alpha)) = D_2^*(\alpha)|_{\alpha=\pi} = 2a + c. \quad (\text{A.6})$$

If $\alpha \in (-\pi, \alpha_4^* - 2\pi]$, we have $D_7 < D_2^*(\alpha) \leq D_4$, where

$$D_4 = \max(D_2^*(\alpha)) = D_2^*(\alpha)|_{\alpha=\alpha_4^*-2\pi} = \sqrt{a^2 + b^2} + \sqrt{(a+c)^2 + b^2}. \quad (\text{A.7})$$

Area A4: $\alpha_4^* - 2\pi < \alpha \leq \alpha_1^*$

By studying the first and second derivatives of the function $D_2^*(\alpha)$ again, as was done for the Area A2, we can obtain the range of $D_2^*(\alpha)$ for $\alpha_4^* - 2\pi < \alpha \leq \alpha_1^*$. It is found that the function $D_2^*(\alpha)$ has a minimum value at the fixed angle $\alpha = -\pi - \arctan \frac{2b}{c}$, i.e.,

$$D_8 = \min(D_2^*(\alpha)) = D_2^*(\alpha)|_{\alpha=-\pi-\arctan \frac{2b}{c}} = \sqrt{4b^2 + c^2}. \quad (\text{A.8})$$

Within the range $(\alpha_4^* - 2\pi, -\pi - \arctan \frac{2b}{c})$, $D_2^*(\alpha)$ decreases with increasing α . Thus, we have $D_8 \leq D_2^*(\alpha) < D_4$. The function increases with increasing α within the range $(-\pi - \arctan \frac{2b}{c}, \alpha_1^*]$ and the maximum value is taken at the angle $\alpha = \alpha_1^*$. Thus, we have $D_8 < D_2^*(\alpha) \leq D_2$. ■

An example of the above analysis is illustrated in Fig. 8. From Fig. 8, we can see that D_6 is the minimum value of the function $D_2^*(\alpha)$. For a given value of path length $|c| < D < D_6$, we can conclude that all AoAs $\alpha \in (-\pi, \pi]$ fulfil the inequality $D \leq D_2^*(\alpha) < D_6$. However, if the propagation distance $D_6 < D < D_8$, the inequality $D < D_2^*(\alpha)$ can only be satisfied if $\alpha \in [-\pi, \alpha_1] \cup [\alpha_2, \pi)$, where α_1 and α_2 can be obtained by solving the equation $D_2^*(\alpha) = D$. As both α_1 and α_2 are within the subdomain (α_2^*, α_3^*) (see Fig. 8), we choose the second sub-function of (14) as the left-hand side of above equation.

The AoAs α_i ($i = 3, \dots, 8$) can be determined similarly by solving the equation $D_2^*(\alpha) = D$. The expression for $D_2^*(\alpha)$ in the equation is selected based on the range of α_i . For instance, as $\alpha_5 \in (\alpha_1^*, \alpha_2^*)$, the first sub-function of (14) should be used.

ACKNOWLEDGMENT

We gratefully acknowledge the Regional Research Fund of Norway (RFF) for supporting our research.

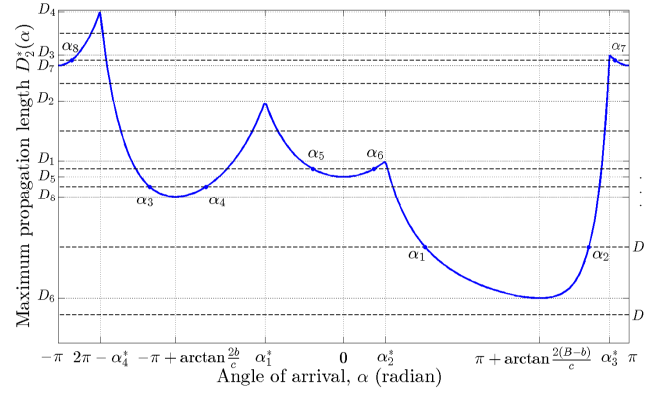


Fig. 8: An example of the relationship between $D_2^*(\alpha)$ and α ($A = 20$ m, $B = 10$ m, $a = 15$ m, $b = 6$ m, $c = -6$ m).

REFERENCES

- [1] E. Tanghe, D. Gaillot, M. Liénard, L. Martens, and W. Joseph, "Experimental analysis of dense multipath components in an industrial environment," *IEEE Transactions on Antennas and Propagation*, vol. 62, no. 7, pp. 3797–3805, 2014.
- [2] E. Tanghe, W. Joseph, J. De Bruyne, L. Verloock, and L. Martens, "The industrial indoor channel: statistical analysis of the power delay profile," *AEÜ-International Journal of Electronics and Communications*, vol. 64, no. 9, pp. 806–812, 2010.
- [3] J. Karedal, S. Wyne, P. Almers, F. Tufvesson, and A. F. Molisch, "A measurement-based statistical model for industrial ultra-wideband channels," *IEEE Transactions on Wireless Communications*, vol. 6, no. 8, pp. 3028–3037, 2007.
- [4] M. Gan, F. Mani, F. Kaltenberger, C. Oestges, and T. Zemen, "A ray tracing algorithm using the discrete prolate spheroidal subspace," in *Proc. of IEEE International Conference on Communications (ICC)*, 2013, pp. 5710–5714.
- [5] S. Beygi, E. G. Ström, and U. Mitra, "Geometry-based stochastic modeling and estimation of vehicle to vehicle channels," in *Proc. of IEEE International Conference on Acoustics, Speech and Signal Processing (ICASSP)*, 2014, pp. 4289–4293.
- [6] M. Naderi, M. Pätzold, and A. G. Zajic, "A geometry-based channel model for shallow underwater acoustic channels under rough surface and bottom scattering conditions," in *Proc. of IEEE International Conference on Communications and Electronics (ICCE)*, 2014, pp. 112–117.
- [7] M. Pätzold, B. O. Hogstad, and N. Youssef, "Modeling, analysis, and simulation of MIMO mobile-to-mobile fading channels," *IEEE Transactions on Wireless Communications*, vol. 7, no. 2, pp. 510–520, 2008.
- [8] L. Jiang and S. Y. Tan, "Geometrically based statistical channel models for outdoor and indoor propagation environments," *IEEE Transactions on Vehicular Technology*, vol. 56, no. 6, pp. 3587–3593, 2007.
- [9] S. Miller and D. Childers, *Probability and Random Processes: With Applications to Signal Processing and Communications*. Elsevier, 2004.
- [10] A. F. Molisch, *Wireless Communications*, 2nd ed. John Wiley & Sons, 2011.
- [11] M. Pätzold, *Mobile Radio Channels*. John Wiley & Sons, 2011.
- [12] C. A. Gutiérrez and M. Pätzold, "The design of sum-of-cisoids Rayleigh fading channel simulators assuming non-isotropic scattering conditions," *IEEE Transactions on Wireless Communications*, vol. 9, no. 4, pp. 1308–1314, 2010.
- [13] J. H. Kwon, H. G. Hwang, J. Y. Kim, C.-B. Chae, and K. S. Kim, "Channel parameter extraction methodology for system-level simulator in small cell environments," in *Proc. of The Sixth International Workshop on Signal Design and Its Applications in Communications*. IEEE, 2013, pp. 99–102.
- [14] Y. Ma and M. Pätzold, "Modeling and statistical characterization of wideband indoor radio propagation channels," in *Proc. of 2010 International Congress on Ultra Modern Telecommunications and Control Systems and Workshops (ICUMT)*. IEEE, pp. 777–783.
- [15] A. Meijerink and A. F. Molisch, "On the physical interpretation of the Saleh-Valenzuela model and the definition of its power delay profiles," *IEEE Transactions on Antennas and Propagation*, vol. 62, no. 9, pp. 4780–4793, 2014.